energies

MDPI

Article

Optimization of a Membraneless Microfluidic Fuel Cell with a Double-Bridge Flow Channel

Ji-Hyun Oh, Tien-Dung Vuong and Kwang-Yong Kim *

Department of Mechanical Engineering, Inha University, 100 Inha-ro, Michuhol-gu, Incheon 22212, Korea; 22201217@inha.edu (J.-H.O.); vuongtien97bkhn@gmail.com (T.-D.V.)
* Correspondence: kykim@inha.ac.kr; Tel.: +82-32-872-3096

Abstract: In this work, a design optimization study was conducted to improve the performance of a membraneless microfluidic fuel cell with a double-bridge cross-section of the flow channel. Governing equations including Navier–Stokes, mass-transport, and Butler–Volmer equations were solved numerically to analyze the electrochemical phenomena and evaluate the performance of the fuel cells. Optimization was performed to maximize the peak power density using a genetic algorithm combined with a surrogate model constructed by radial basis neural network. Two sub-channel widths of the flow channel were selected as design variables for the optimization. As a result, a large increase in the inner channel width and a small decrease in the outer channel width effectively increased the peak power density of the MMFC. The optimal design increased the peak power density by 57.6% compared to the reference design.

Keywords: membraneless microfluidic fuel cell; double-bridge channel; numerical model; optimization; mixing region

Citation: Oh, J.-H.; Vuong, T.-D.; Kim, K.-Y. Optimization of a Membraneless Microfluidic Fuel Cell with a Double-Bridge Flow Channel. *Energies* **2022**, *15*, 973. https://doi.org/10.3390/en15030973

Academic Editor: Alexandros Arsalis

Received: 21 December 2021
Accepted: 26 January 2022
Published: 28 January 2022

1. Introduction

Current combustion-based energy generation technology is very harmful to the environment and causes global problems such as ozone-layer depletion and the consistent reduction in vegetation cover resulting from climate change [1]. On the other hand, a fuel cell provides an efficient and clean mechanism as an electrochemical device that can directly convert the chemical energy of fuel into electrical energy [1,2].

Fuel cells are used to generate electricity in some applications, such as spacecraft and emergency generators, and also used as power sources for portable electronic components [3]. A research was conducted for 1–100 mW class applications of fuel cells such as distributed microsensors and wireless micro-electro mechanical systems [4], and fuel cells were introduced into small electric vehicles [5]. Fuel cells can supply electricity together with cogeneration [6]. As the use of renewable energy has been pursued, it is also being used in the field of solar heat and solar power [7]. On-chip integration of fuel cells miniaturizes the reactor and maximizes fuel storage, so they are used in applications with limited form factors, such as wireless sensor nodes [8]. A fuel cell is recommended as a high power source in portable applications due to its active system integrating single cells and stacks, and is used as a power source, such as in chargers, LEDs and small fans [9]. Due to the current increase in various diseases, implantable medical devices and wearable devices are continuously being developed, and fuel cells have been applied to overcome the problems of power generation and replacement [10]. Fuel cells are also used in military equipment because of their high power density, durability, and convenient portability [11].

Recently, as the use of portable electronics has increased, the demand for battery power has also increased, but the existing battery technology cannot keep up with this demand [12]. A fuel cell solely works to generate energy and an additional unit is coupled alongside to store the energy. Thus, in fuel cells, both units can be individually customized

for convenience [13]. In addition, it has the potential of high energy density, low cost, simple design and durability, making it suitable as a portable power system [3].

Most fuel cell structures use a proton-exchange membrane (PEM) to separate fuel and oxidants. Fuel cells operate at higher temperatures due to their fast kinetics, which dries PEM, resulting in a problem of reduction of proton conduction [14]. Membraneless Microfluidic Fuel Cell (MMFC), which can solve this problem, was first suggested in 2002 by Ferrigno et al. [15]. MMFC removes PEM, but can avoid the active mixing between the fuel and the oxidant streams using the laminar flow with a low Reynolds number (Re). A liquid–liquid interface acts like a membrane so that the separate fuel and oxidant streams flow in parallel along the channel. Thus, the MMFC is free from problems such as fouling, damaging, and drying out of the membrane [15], simplifies the structural design, and can merge electrode assembly and bipolar plates into a single substrate [16,17]. In addition, the crossover phenomenon is reduced, and economic efficiency is increased [18]. However, MMFCs generally have a problem of low power density compared to conventional PEM-based fuel cells, due to the relatively long distance between electrodes.

Thus, to enhance the performance of MMFCs, many researchers have conducted various studies on the structure and arrangement of flow channels and electrodes. Tanveer et al. [19] tested and numerically investigated microchannels of an MMFC with tapered and non-tapered electrodes, and obtained an approximately 93% increase in peak power density when tapered electrodes were used. Hollinger et al. [20] reduced the cross-sectional area by incorporating a nanoporous track etch separator at the electrolyte interface to minimize fuel crossover. Sun et al. [21] conducted a study on an MMFC using triple streams of fuel and oxidant to prevent crossover. Montesinos et al. [17] proposed an MMFC with a bridge-type channel cross-section to reduce the crossover of reactants, improve reactant transport and improve fuel utilization. Jayashree et al. [22] investigated a T-type MMFC to improve mass transportation and enhanced the fuel utilization efficiency by 54%. Shyu et al. [23] reduced the residential time of gas bubbles with an H-type MMFC and shortened the catalyst loading by reducing the bubble dimension on the anode surface. Jayashree et al. [24] proposed an F-type MMFC to significantly improve the oxygen reduction reaction rate and to solve the mass transfer issue. Tanveer and Kim [25,26] performed numerical investigations of MMFCs with multiple inlets and various flow channels to improve performance by reducing ohmic losses. Liu et al. [27] proposed a three-dimensional herringbone structure to expand the active site and increase the surface area utilization of the electrode.

Design optimization using systematic optimization algorithms has become a powerful tool for the design of numerous devices involving fluid flow [28]. In particular, optimization techniques based on surrogate modeling have efficiently reduced the computing time in a wide range of applications [29]. Using design optimization, the performance of devices can be maximized under specified constraints. However, application of design optimization to the MMFC design has not yet been found.

Oh et al. [30] proposed a new MMFC structure with a double-bridge channel to further improve the performance of the bridge-shaped MMFC of Montesinos et al. [17], and evaluated its performance by analyzing the electrochemical phenomena in the MMFC channel using a numerical model. The double-bridge MMFC showed 34.0% higher peak power density compared to the single-bridge MMFC, proving its excellent performance. A parametric study was also performed using the sub-channel widths and bridge height as the parameters, which showed that the relative sub-channel widths affected sensitively the peak power density of the MMFC, indicating the need for optimizing the channel geometry.

Therefore, the design of the double-bridge channel of the MMFC was optimized to maximize the performance. This is the first application of systematic optimization techniques to MMFC design. The peak power density was selected as an objective function using two sub-channel widths as the design variables for optimization. A Radial Basis Neural Network (RBNN) was used to construct the surrogate model of the objective function from the numerical results of the sample designs, and a Genetic Algorithm (GA) was utilized to find the optimal design based on the surrogate model. The power density

of the MMFC was obtained from a numerical simulation solving Navier–Stokes, mass-transport, and Butler–Volmer equations.

2. MMFC Geometry

The configuration of the channel and double-bridge channel cross-section of the MMFC to be optimized in this study is shown in Figure 1. As shown in Figure 1a, fuel and oxidant enter the double-bridge channel through the inlets and proceed along the flow path. The length (L_0) of the microchannel is 10 mm, the half width (W) of the channel is 150 μm, and the height (H) of the channel is 50 μm. The channel half-width (W) is divided into three sub-channel widths. The widths of the outer channel, bridge channel, and inner half channel are indicated by W_O, W_B, and W_I, respectively, as shown in Figure 1b. The three sub-channel widths are same at 50 μm, and the reference width is W_r = 50 μm, which is defined to make the sub-widths dimensionless. The bridge height is h = 10 μm. For the optimization, W is fixed at 150 μm with a constraint of $W_B/W_r \geq 0.2$. The design specifications of the reference channel are found in Table 1.

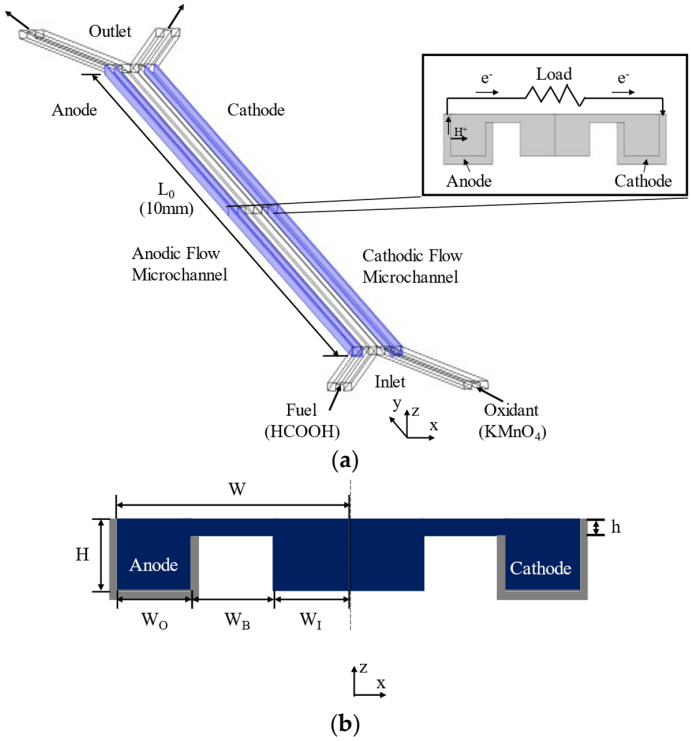

Figure 1. Configuration of double-bridge shaped MMFC channel. (**a**) Flow channel, (**b**) channel cross-section (grey regions indicate electrodes) [30].

Table 1. Specifications of the reference channel.

Parameter	Value
Length of the micro channel (L_0), mm	10
Channel half-width (W), μm	150
Channel height (H), μm	50
Outer channel width (W_O), μm	50
Bridge channel width (W_B), μm	50
Inner channel half-width (W_I) μm	50
Bridge height width (h), μm	10
Reference width (W_r), μm	50
Flow rate, μL/min	60

3. Numerical Analysis

Due to the low Reynolds number in the MMFC channel, the flow is laminar. To simplify the electrochemical analysis and the numerical model, it was assumed that the temperature and density of the working fluids are constant and the flow is steady. It was also assumed that the depletion region does not have a significant effect on the thickest mixed region at the outlet of the flow path. For the numerical investigation, the commercial computational fluid dynamics (CFD) software COMSOL Multiphysics® (version 4.3, COMSOL, Inc., Stockholm, Sweden) [31] was used.

Due to the high energy density and convenient storage, liquid reactants have been used in numerous studies on MMFCs [14,32–34]. In this study, formic acid (*HCOOH*) and potassium permanganate ($KMnO_4$) were used as the fuel and oxidant, respectively. Formic acid as a fuel promotes electron and proton transport within the anode compartment of the fuel cell [35]. Potassium permanganate as an oxidizing agent also improves cathode dynamics and makes it possible to generate higher power densities than air [14].

The electrochemical reaction of the anode is as follows:

$$HCOOH \rightarrow CO_2 + 2H^+ + 2e^- \quad (1)$$

In addition, the primary permanganate reduction occurring at the cathode is as follows:

$$MnO_4^- + 8H^+ + 5e^- \rightarrow Mn^{2+} + 4H_2O \quad (2)$$

The permanganate ion is further oxidized to insoluble MnO_2 by the following reaction:

$$2MnO_4^- + 3Mn^{2+} + 2H_2O \rightarrow 5MnO_2 + 4H^+ \quad (3)$$

The reactants were transported downstream along the channel by convection. Fick's law of diffusion was used to decide the transport of reactants in the MMFC channel [36]. In the numerical model, it was assumed that flows are isothermal, and pressure differences are not large enough. Implementing these assumptions allows the concentration distributions of the fuel and oxidant to be described by Fick's law [37]. Fick's law predicts variation in the concentration of reactant species with time along the channel caused by the diffusion.

$$\nabla \cdot (-\mathrm{D}_i \nabla \mathrm{C}_i + \mathrm{C}_i \mathbf{u}) = 0 \quad (4)$$

where **u** is velocity vector, D_i is the diffusion coefficient, and C_i is the local concentration for species *i*. In the electrode subdomains, a source term is added to the above equation to accommodate the consumption of species by electrochemical reactions. This results in the following equation:

$$\nabla \cdot (-\mathrm{D}_i \nabla \mathrm{C}_i + \mathrm{C}_i \mathbf{u}) = S_i \quad (5)$$

where the source term (S_i) is calculated by Butler–Volmer equations.

The electrochemical reactions in the MMFC were modelled using the Butler–Volmer equations [36]. Additionally, the reactants consumed by the electrode were calculated using Faraday's law. The concentration of ions (i.e., H^+ or OH^-) was assumed to be constant in the flow channel [38]. The Butler–Volmer, Navier–Stokes, and convection–diffusion equations were combined to predict the current density for a specified cell voltage. At the channel inlet, constant concentration and cell pressure drop are specified. Additionally, at the channel outlet, constant pressure and mass flux are specified. In addition, no-slip conditions were specified on the wall of the channel.

Previous simulations of MMFCs generally introduced a single-phase flow assumption, and the present computational model also used the single-phase assumption. The formation of gas bubbles (e.g., O_2 and CO_2) was neglected, and it was supposed that the bubbles formatted at the anode are fully dissolved in the electrolyte [17,19,39–42]. Wang et al. [43] and Shyu et al. [44] studied two-phase numerical models to confirm the effects of bubble

formation on the performance of an MMFC. More detailed information on the numerical model can be found in ref. [30].

4. Optimization Technique

4.1. Design Variables

Selection of proper design variables is important in optimization. Thus, a parametric study must be performed to find the parameters affecting the objective function. When the range of each design variable is narrowed, the accuracy of the surrogate model constructed for the objective function increases for the same number of sample designs. In the previous work [30], a parametric study was conducted to find the important parameters for the design of the double-bridge MMFC among the sub-channel widths, W_I, W_B and W_O with fixed $W/W_r = 3.0$. The results indicated that the power density is relatively insensitive to W_B among the three parameters. When $W_I/W_r = 1.7$ ($W_O/W_r = 0.3$) with fixed $W_B/W_r = 1.0$, the peak power density increased by about 18% compared to the reference design. As W_I increased, the mixing layer became thinner, reducing ohmic loss. The results of the parametric study [30] with fixed W_B are summarized in Table 2 and Figure 2. The overall results of the parametric study [30] indicated that W_I is the most critical parameter and W_O is the second important parameter in terms of sensitivity of the peak power density, and these two parameters were selected as design variables for the present optimization.

Table 2. Results of a previous parametric study [30] when W and W_B were fixed ($W_B/W_r = 1.0$).

$\frac{W_I}{W_r}$-$\frac{W_B}{W_r}$-$\frac{W_O}{W_r}$	W_I-W_B-W_O (μm)	Peak Power Density (mW/cm^2)	Relative Increase (%)
1.7-1-0.3	85-50-15	37.75	18.4
1.3-1-0.7	65-50-35	33.98	6.6
1-1-1 (Reference)	50-50-50	31.88	-
0.7-1-1.3	35-50-65	30.27	−5.0
0.4-1-1.6	20-50-80	29.16	−8.5

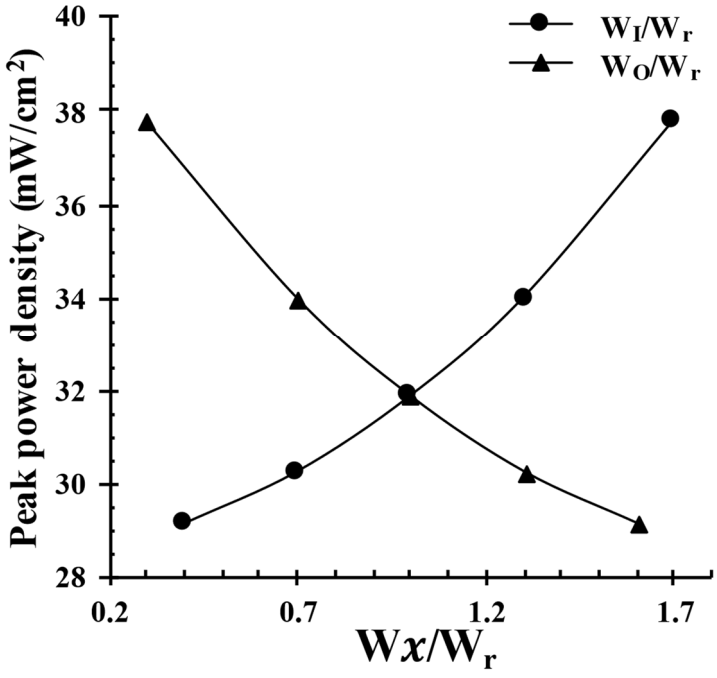

Figure 2. Variations of peak power density with W_I and W_O for fixed W and W_B ($W_B/W_r = 1.0$).

Table 3 shows the design ranges of the two design variables. In the optimization, the following two design constraints must be satisfied:

$$W_B/W_r \geq 0.2 \quad (6)$$

$$W_I + W_B + W_O = 3.0\ Wr \quad (7)$$

Table 3. Design variables and ranges.

Design Variable	W_I/W_r	W_O/W_r
Upper Limit	2.50	1.50
Reference Value	1.00	1.00
Lower Value	1.00	0.30

The first constraint secures the minimum width of the bridge structure, which consists of the electrode and supporting structure. The second constraint indicates that the overall width of the channel remains constant for the optimization.

4.2. Optimization Methodology

The present optimization goal is to maximize the peak power density of the double-bridge MMFC. Figure 3 illustrates the present optimization procedure based on surrogate modeling.

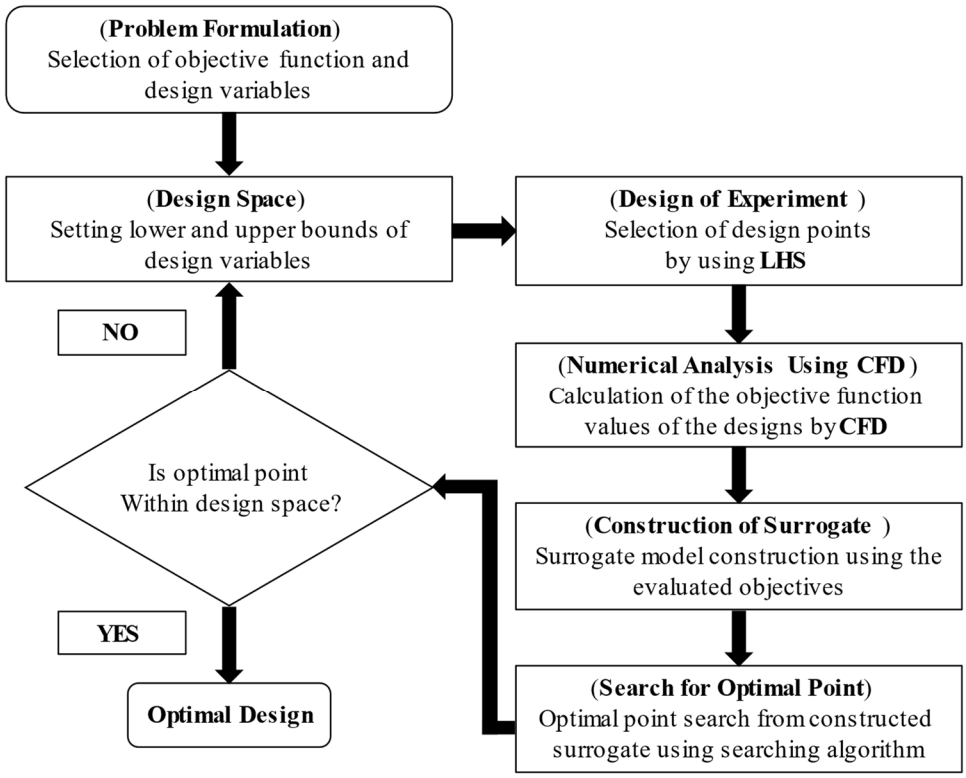

Figure 3. Optimization procedure.

The optimization problem can be defined as:

$$\text{Maximization} : F(\boldsymbol{x}) = \textit{Peak Power Density} \quad (8)$$

$$\text{Design variable bound} : LB_i \leq x_i \leq UB_i,\ \boldsymbol{x} \in R$$

Here, $F(\boldsymbol{x})$ is the objective function, i.e., the *peak power density*, $\boldsymbol{x}(= \{x_i\})$ is a vector of n design variables, and LB_i and UB_i are the lower and upper limits, respectively.

4.2.1. Design of Experiment

Latin hypercube sampling (LHS) [45] was employed to select design points (or sample points) in the design space. Twenty design points for the two design variables (W_I and W_O) were generated using the *lhsdesign* function in MATLAB [46] (MathWorks, Inc., Natick, MA, USA). The LHS technique is a sampling technique that reduces time by using an m×n simulation matrix and can efficiently analyze variable space at a minimum cost. Here, m is the number of samples to be extracted and n is the number of variables. Additionally, this method is designed to represent all parts of the design space and generate random sample points. After removing sample designs that did not fit the constraints, the remaining nine sample designs were used for evaluating the objective function. Table 4 lists the numerical results of the nine sample designs.

Table 4. Design variables and objective function values at sample designs.

Design	W_I/W_r	W_O/W_r	Peak Power Density (mW/cm^2)
1	1.5209	0.97997	41.335
2	1.5805	1.1222	46.288
3	1.1058	1.1641	35.084
4	1.0165	0.70626	30.444
5	2.1537	0.34418	47.136
6	1.6642	0.38932	37.610
7	1.3213	0.52709	24.165
8	2.0199	0.45923	45.257
9	1.9220	0.81518	49.853

4.2.2. Radial Basis Neural Network

RBNN [47] was used to construct the surrogate model. RBNN is an artificial neural network that uses radial basis functions as activation functions, and has many uses, including function approximation, time series prediction, classification, and system control. The RBNN model includes the output layer of linear neurons, as well as the hidden layer of radial neurons. The hidden layer uses radial primitives to transform the input space into an intermediate space. The output of hidden layers is passed to a combiner to create targets. In MATLAB, a RBNN model was created using *newrb* function with the input being the obtained data of the design of the experiment.

4.2.3. Searching Algorithms

GA [48] was selected as the searching algorithm in the present work. GA finds the maximum of a function by mimicking biological evolutionary processes. This method randomly selects chromosomes before starting and sets the initial population size. Subsequent computations allow one chromosome to adapt in a competitive way. Chromosomes selected after the start of computation are called parental generation, and those selected after parental generation are called child generation. By genetic search operators (selection, crossover, and mutation), chromosomes that are superior to those of the previous generation are extracted. In MATLAB [46], single-objective optimization using GA can be performed using a function.

5. Results and Discussion

5.1. Grid Convergence Index Analysis and Validation of Numerical Results

To evaluate the grid-dependency of the numerical results, the Grid Convergence Index (GCI) analysis for the MMFC current was performed using Richardson extrapolation [49] in the previous work [30]. Table 5 summarizes the GCI analysis results. To adjust the number of nodes, the grid segmentation index was set to 1.3. The current of MMFC shows a tendency to converge gradually as the number of grid nodes increased, as can be seen in Figure 4. Extrapolated relative error (when using N_1) e_{ext}^{21} is 0.131%, and GCI_{fine}^{21} is

0.163%, indicating that the numerical uncertainty is sufficiently small. Consequently, N_1 was selected as the final grid system. Additional calculations were performed based on the structure of this grid. A tetrahedral mesh was generated in the designated computational domain, and the mesh was generated using the physics-controlled mesh option built in COMSOL. A mesh created in the boundary layer was composed of fine elements.

Table 5. Grid convergence index (GCI) analysis for the MMFC current [30].

Parameters		Values
Number of cells	N_1 N_2 N_3	3341,684 1366,550 688,043
Grid refinement factor	r	1.3
Currents corresponding to N_1, N_2, and N_3 (mA)	φ_1 φ_2 φ_3	0.5244 0.5281 0.5339
Apparent order	P	2.0762
Extrapolated values	$\varnothing_{ext}^{21}$	52.37%
Approximate relative error	e_a^{21}	0.706%
Extrapolated relative error	e_{ext}^{21}	0.131%
Grid convergence index	GCI_{fine}^{21}	0.163%

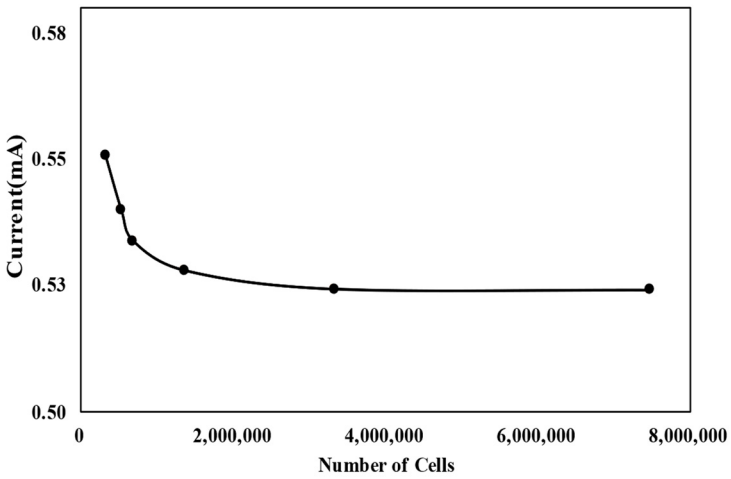

Figure 4. Grid-dependency test for MMFC current [30].

To validate the numerical results, the predicted performance curves for the single-bridge channel were compared with the experimental data measured by Montesinos et al. [17] by Oh et al. [30] using the same numerical model as in the present work, as shown in Figure 5. Compared with the experimental data, Figure 5a shows the lowest relative error of 0.65% at 0.7 V. Overall, good agreement can be seen between the numerical and experimental data. In the power density versus current density curve (Figure 5b), the numerical results somewhat differ from the previous experimental results at lower cell voltages. However, the MMFC functioned at a nominal cell voltage between 0.6 and 0.8 V. It was confirmed that it was in good agreement with the experimental results. The OCP (Open Circuit Potential) in this study is 1.4 V. However, the typical OCP is in a range of 0.6~1.2 V. The difference is due to the high oxidation and reduction potential of $KMnO_4$. Other studies have also confirmed cases with higher OCP. Wang et al. [50] summarized MMFCs investigated with various reactants, and highlighted the impact of fuel and oxidant combination on OCP. Furthermore, it also varies with the nature of electrolyte. Various studies have highlighted

that a dual-electrolyte configuration (acidic-alkaline) results in higher OCP. Liu et al. [51] employed the acid-alkaline dual-electrolyte together with $KMnO_4$ as an oxidant. The cell OCV was as high as 1.83 V.

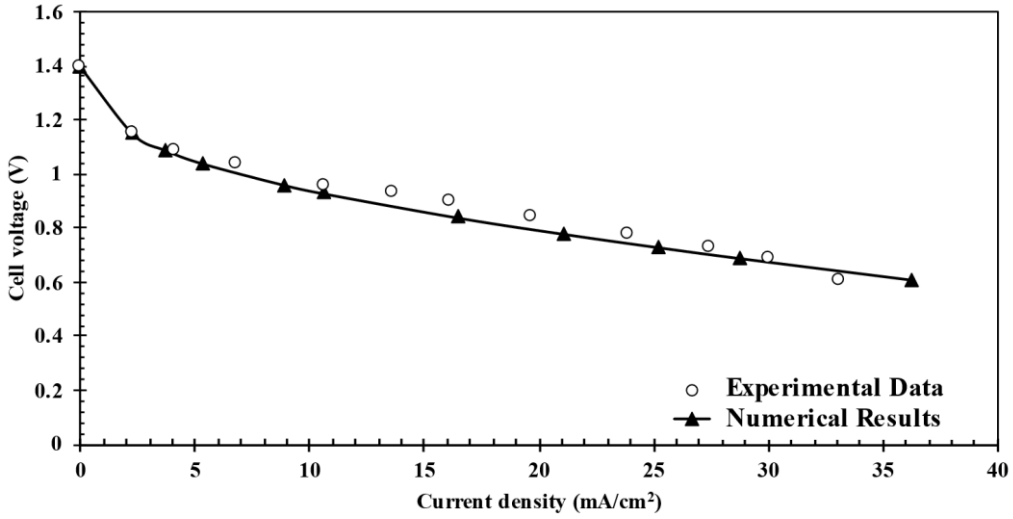

(**a**)

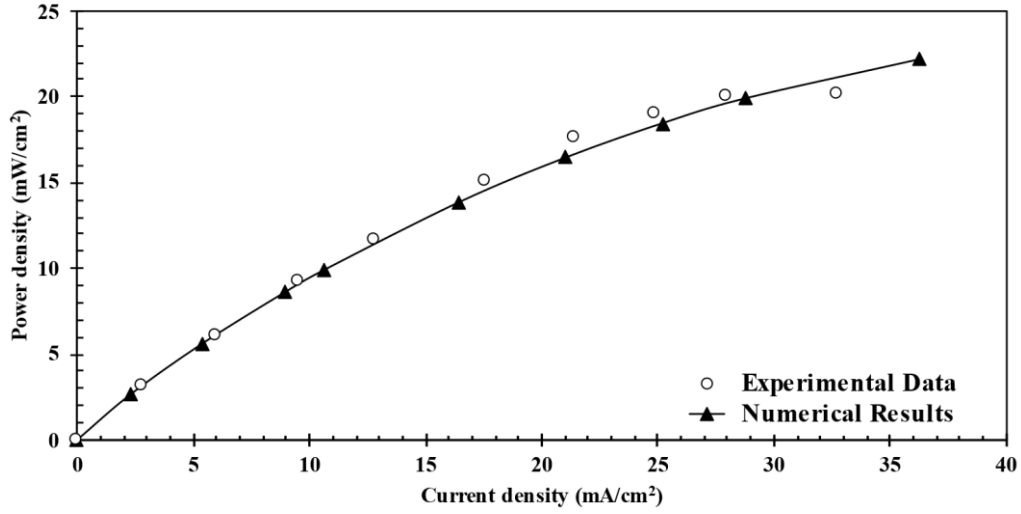

(**b**)

Figure 5. Validation of the predicted performance curves [30] using experimental data of Montesinos et al. [17]. (**a**) Cell voltage; (**b**) power density.

5.2. Optimization Results

From the RBNN model constructed for the objective function, GA found the optimal design of the double-bridged MMFC at $W_I/W_r = 1.922$ ($W_I = 96.1$ μm) and $W_O/W_r = 0.815$ ($W_O = 40.7$ μm) as shown in Table 6. The W_B value of the optimal design ($W_B/W_r = 0.263$) is located near the design limit, indicating the minimum thickness of the bridge structure. The optimum value of W_I is more than twice as large as the optimum value of W_O, which indicates that the effect of W_I on the power density is far larger than that of W_O. The predicted optimized peak power density is 49.85 mW/cm^2 while the CFD result is 50.24 mW/cm^2, which yielded a relative error of only 0.77%. This small error proves that the use of the RBNN model and GA is suitable for the investigated problem. In terms of improvement from the reference design, the optimal design increased the peak power density significantly by 57.6% from that of the reference design. Figure 6 shows the peak

power density curves for the reference and optimal designs of the double-bridge MMFC, which confirms the achievement of the optimization.

Table 6. Results of optimization.

	W_I/W_r	W_O/W_r	Peak Power Density (mW/cm^2)		Error (%)	Improvement (%)
			Prediction	CFD		vs. Reference
Reference design	1.0	1.0	-	31.88	-	-
Optimal design	1.922	0.815	49.85	50.24	0.77	57.6

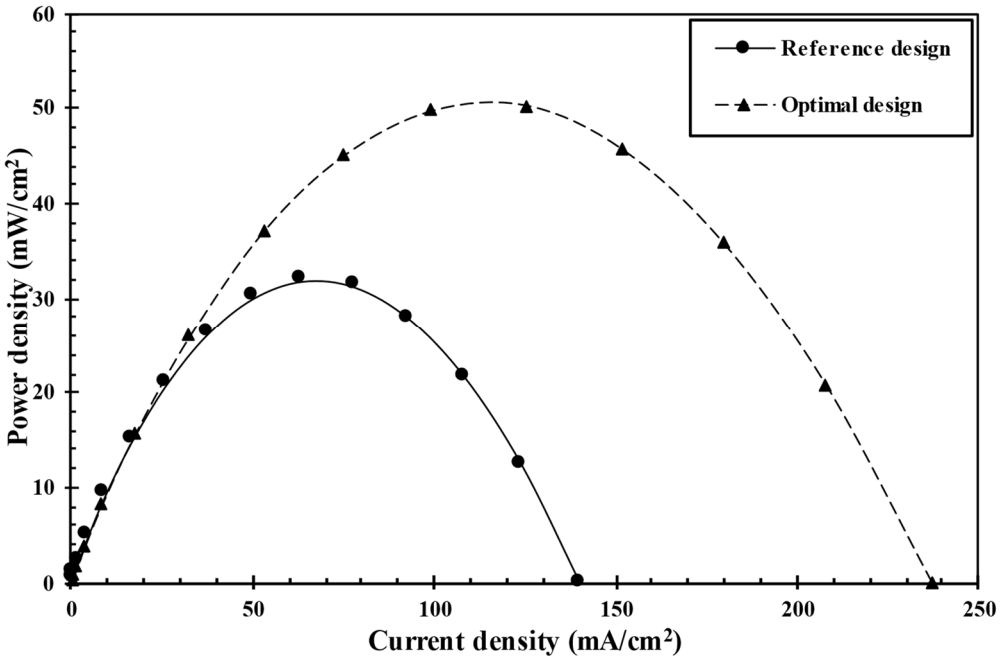

Figure 6. Comparison of performance curves between reference and optimal designs of double-bridge MMFC.

In Figure 7, the oxidant ($KMnO_4$) concentration contours of the reference [30] and optimized designs are plotted in the x-z plane 5 mm downstream of the channel inlet. As can be seen in this figure, it is confirmed that the optimal design has an increased inner channel half-width (W_I) and a decreased outer channel width (W_O) compared to the reference design, which makes the depletion region around each electrode thicker and the mixing region in the inner channel thinner. Therefore, due to the decreased thickness of the mixing region, proton transportation across the mixing layer is promoted, which reduces ohmic losses, and makes the consumption of reactants faster and more efficient. Due to the increase in the width of the inner channel, the distance between the mixing and depletion layers is also increased, and thus the possibility of crossover is reduced in the optimal design. As a sufficient oxidant reaches the activation wall of the channel with optimization, the depletion region expands, increasing mass transportation losses. However, due to the fast reaction rate and reduction of ohmic losses, protons migrated efficiently through the mixing region, resulting in higher current generation and increased peak power density. This was confirmed to be effective in overcoming mass transport losses.

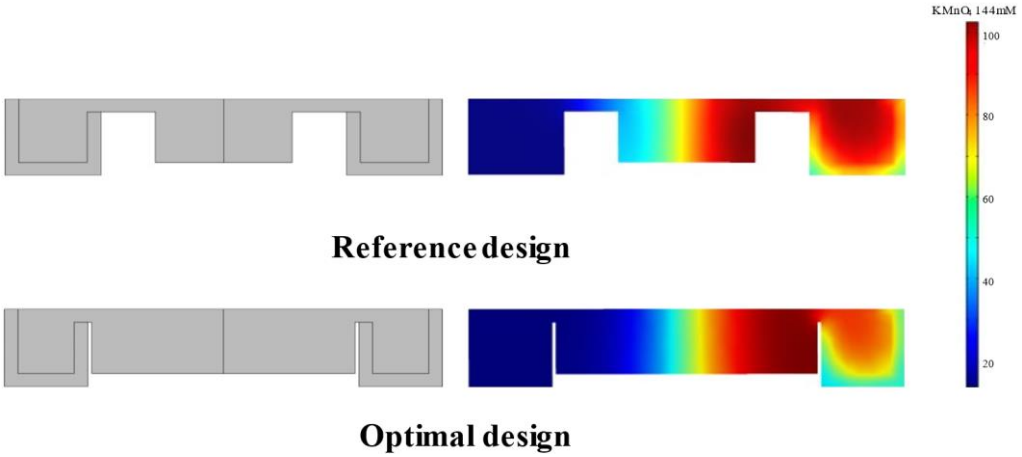

Figure 7. Comparison of oxidant ($KMnO_4$) concentration contours on x-z plane 5 mm downstream of the channel inlet between reference design [30] and optimal design.

6. Conclusions

The present work optimized the flow channel configuration of the double-bridge MMFC, which showed far better performance than the MMFC employing single-bridge structure for the channel cross-section. To develop clear insight into the impact of depletion regions and mixing regions on the performance of the MMFC, a single-phase numerical model was used. The surrogate-based optimization was performed using GA combined with the RBNN model to maximize the objective function, i.e., the peak power density. The inner channel width (W_I) and outer channel width (W_O) of the double-bridge channel were selected as design variables for optimization. The optimal design was found at $W_I/W_r = 1.922$ and $W_O/W_r = 0.815$. The results for the objective function predicted by the RBNN model and calculated by CFD analysis at the optimal design showed a very small error of 0.77%, confirming the validity of the employed optimization methods. Compared to the reference design, the peak power density was increased by 57.6% (50.24 mW/cm^2) through the optimization. The concentration contours showed that the thickness of the mixing layer in the inner channel decreased, largely reducing ohmic losses by the optimization, but the mass transportation losses increased and the depletion region expanded even though the overall performance was enhanced. Therefore, further research is needed to reduce mass transportation losses in the optimized double-bridge MMFC.

Author Contributions: J.-H.O.: numerical analysis, writing—original draft, T.-D.V.: optimization, writing—original draft, K.-Y.K.: writing—review and editing, supervision, funding acquisition. All authors have read and agreed to the published version of the manuscript.

Funding: This work was supported by the National Research Foundation of Korea (NRF) grant funded by the Korean government (MSIT) (No. 2019R1A2C1007657).

Institutional Review Board Statement: Not applicable.

Informed Consent Statement: Not applicable.

Data Availability Statement: Not applicable.

Conflicts of Interest: The authors declare no conflict of interest.

References

1. Omar, Z.; Sharaf; Mehmet, F.; Orhan. An overview of fuel cell technology: Fundamentals and applications. *Renew. Sustain. Energy Rev.* **2014**, *32*, 810–853.
2. Kamarudin, S.K.; Daud, W.R.W.; Som, A.M.; Takriff, M.S.; Mohammad, A.W.; Loke, Y.K. Design of a fuel processor unit for PEM fuel cell via shortcut design method. *Chem. Eng. J.* **2004**, *104*, 7–17. [CrossRef]
3. Tabbi, W.; Alaswad, A.; Palumbo, A.; Dassisti, M.; Olabi, A.G. Advances in stationary and portable fuel cell applications. *Int. J. Hydrogen Energy* **2016**, *41*, 16509–16522.

4. Motokawa, S.; Mohamedi, M.; Momma, T.; Shoji, S.; Osaka, T. MEMS-based design and fabrication of a new concept micro direct methanol fuel cell (l-DMFC). *Electrochem. Commun.* **2004**, *6*, 562–565. [CrossRef]
5. Goor, M.; Menkin, S.; Peled, E. High power direct methanol fuel cell for mobility and portable applications. *Int. J. Hydrogen Energy* **2019**, *44*, 3138–3143. [CrossRef]
6. Pan, Z.F.; Chen, R.; An, L.; Li, Y.S. Alkaline anion exchange membrane fuel cells for cogeneration of electricity and valuable chemicals. *J. Power Sources* **2017**, *365*, 430–445. [CrossRef]
7. Adhami, H. Designing and analysis of the micro-trigeneration systems based on combined proton exchange membrane fuel cell with photovoltaic and photovoltaic/thermal prime movers in portable applications. *Appl. Therm. Eng.* **2020**, *180*, 115779. [CrossRef]
8. Xiao, Z.Y.; Feng, C.H.; Chan, P.C.H.; Hsing, I.M. Monolithically integrated planar microfuel cell arrays. *Sens. Actuators B* **2008**, *132*, 576–586. [CrossRef]
9. Alias, M.S. Active direct methanol fuel cell: An overview. *Int. J. Hydrogen Energy* **2020**, *45*, 19620–19641. [CrossRef]
10. Singh, R. Bio-compatible bio-fuel cells for medical devices. *Mater. Today Proc.* **2021**, *44*, 242–249. [CrossRef]
11. Patil, A.; Dubois, T.G.; Sifer, N.; Bostic, E.; Gardner, K.; Quah, M.; Bolton, C. Portable fuel cell systems for America's army: Technology transition to the field. *J. Power Sources* **2004**, *136*, 220–225. [CrossRef]
12. Dyer, C.K. Fuel cells for portable applications. *J. Power Sources* **2002**, *106*, 31–34. [CrossRef]
13. Lee, S.J.; Chang-Chien, A.; Cha, S.W.; O'Hayre, R.; Park, Y.I.; Saito, Y.; Prinz, F.B. Design and fabrication of a micro fuel cell array with "flip-flop" interconnection. *J. Power Sources* **2002**, *112*, 410–418. [CrossRef]
14. Choban, E.R.; Markoski, L.J.; Wieckowski, A.; Kenis, P.J.A. Microfluidic fuel cell based on laminar flow. *J. Power Sources* **2004**, *128*, 54–60. [CrossRef]
15. Ferrigno, R.; Stroock, A.D.; Clark, T.D.; Mayer, M.; Whitesides, G.M. Membraneless Vanadium Redox Fuel Cell Using Laminar Flow. *J. Am. Chem. Soc.* **2002**, *124*, 12930–12931. [CrossRef]
16. Choban, E.R.; Spendelow, J.S.; Gancs, L.; Wieckowski, A.; Kenis, P.J.A. Membraneless laminar flow-based micro fuel cells operating in alkaline, acidic, and acidic/alkaline media. *Electrochim. Acta* **2005**, *50*, 5390–5398. [CrossRef]
17. López-Montesinos, P.O.; Yossakda, N.; Schmidt, A.; Brushett, F.R.; Pelton, W.E.; Kenis, P.J.A. Design, fabrication, and characterization of a planar, silicon-based, monolithically integrated micro laminar flow fuel cell with a bridge-shaped microchannel cross-section. *J. Power Sources* **2001**, *196*, 4638–4645. [CrossRef]
18. Hanapi, I.H.; Kaarudin, S.K.; Zainoodin, A.M.; Hasran, U.A. Memrane-less micro fuel cell system design and performance: An overview. *Int. J. Energy Res.* **2019**, *43*, 8956–8972. [CrossRef]
19. Tanveer, M.; Kim, K.Y. Effects of geometric configuration of the channel and electrodes on the performance of a membraneless micro-fuel cell. *Energy Convers. Manag.* **2017**, *136*, 372–381. [CrossRef]
20. Hollinger, A.S.; Maloney, R.J.; Jayashree, R.S.; Natarajan, D.; Markoski, L.J.; Kenis, P.J.A. Nanoporous separator and low fuel concentration to minimize crossover in direct methanol laminar flow fuel cells. *J. Power Sources* **2010**, *195*, 3523–3528. [CrossRef]
21. Sun, M.H.; Velve Casquillas, G.; Guo, S.S.; Shi, J.; Ji, H.; Ouyang, Q.; Chen, Y. Characterization of microfluidic fuel cell based on multiple laminar flow. *Microelectron. Eng.* **2007**, *84*, 1182–1185. [CrossRef]
22. Jayashree, R.S.; Yoon, S.K.; Brushett, F.R.; Lopez-Montesinos, P.O.; Natarajan, D.; Markoski, L.J.; Kenis, P.J.A. On the performance of membraneless laminar flow-based fuel cells. *J. Power Sources* **2010**, *195*, 3569–3578. [CrossRef]
23. Shyu, J.C.; Wang, P.Y.; Lee, C.L.; Chang, S.C.; Sheu, T.S.; Kuo, C.H.; Huang, K.L.; Yang, Z.Y. Fabrication and Test of an Air-Breathing Microfluidic Fuel Cell. *Energies* **2015**, *8*, 2082–2096. [CrossRef]
24. Jayashree, R.S.; Gancs, L.; Choban, E.R.; Primal, A.; Natarajan, D.; Markoski, L.; Kenis, P.J.A. Air-Breathing Laminar Flow-Based Microfluidic Fuel Cell. *J. Am. Chem. Soc.* **2005**, *127*, 16758–16759. [CrossRef] [PubMed]
25. Tanveer, M.; Kim, K.Y. Performance analysis of a micro laminar flow fuel cell with multiple inlets of a bridge-shaped microchannel. *J. Power Sources* **2018**, *399*, 8–17. [CrossRef]
26. Tanveer, M.; Kim, K.Y. Effects of Bridge-Shaped Microchannel Geometry on the Performance of a Micro Laminar Flow Fuel Cell. *Micromachines* **2019**, *10*, 822. [CrossRef] [PubMed]
27. Liu, Z.; Ye, D.; Chen, R.; Zhang, B.; Zhu, X.; Liao, Q. A dual-functional three-dimensional herringbone-like electrode for a membraneless microfluidic fuel cell. *J. Power Sources* **2019**, *438*, 227058. [CrossRef]
28. Kim, K.Y.; Abdus, S.; Ernesto, B. *Design Optimization of Fluid Machinery (Applying Computational Fluid Dynamics and Numerical Optimization)*; John Wiley & Sons Pte. Ltd.: Singapore, 2019; 304p, ISBN 9781119188292.
29. Arshad, A.; Kim, K.Y. *Analysis and Design Optimization of Micromixers*; SpringerBriefs in Computational Mechanics; Springer Nature Singapore Pte Ltd.: Singapore, 2021; 75p, ISBN 9789813342903. [CrossRef]
30. Oh, J.H.; Tanveer, M.; Kim, K.Y. A Double-Bridge Channel Shape of a Membraneless Microfluidic Fuel Cell. *Energies* **2021**, *14*, 6973. [CrossRef]
31. COMSOL AB. *COMSOL Multiphysics Reference Guide*; Version 4.3; COMSOL, Inc.: Stockholm, Sweden, 2012; Available online: www.comsol.com (accessed on 26 November 2019).
32. Kjeang, E.; Djilali, N.; Sinton, D. Microfluidic fuel cells: A review. *J. Power Sources* **2009**, *186*, 353–369. [CrossRef]
33. Shaegh, S.A.M.; Nguyen, N.T.; Chan, S.H. A review on membraneless laminar flow-based fuel cells. *Int. J. Hydrogen Energy* **2011**, *36*, 5675–5694. [CrossRef]

34. Tanveer, M.; Lim, E.S.; Kim, K.Y. Effects of channel geometry and electrode architecture on reactant transportation in membraneless microfluidic fuel cells: A review. *Fuel* **2021**, *298*, 120818. [CrossRef]
35. Rice, C.; Ha, S.; Masel, R.I.; Waszczuk, P.; Wieckowski, A.; Barnard, T. Direct formic acid fuel cells. *J. Power Sources* **2002**, *111*, 83–89. [CrossRef]
36. Ni, M.; Leung, M.K.H.; Leung, D.Y.C. Parametric study of solid oxide fuel cell performance. *Energy Convers. Manag.* **2007**, *48*, 1525–1535. [CrossRef]
37. Jayakumar, A. A technical review on gas diffusion, mechanism and medium of PEM fuel cell. *Ionics* **2015**, *21*, 1–18. [CrossRef]
38. Khabbazi, A.E.; Richards, A.J.; Hoorfar, M. Numerical study of the effect of the channel and electrode geometry on the performance of microfluidic fuel cells. *J. Power Sources* **2010**, *195*, 8141–8151. [CrossRef]
39. Shaegh, S.A.M.; Nguyen, N.T.; Chan, S.H. An air-breathing microfluidic formic acid fuel cell with a porous planar anode: Experimental and numerical investigations. *J. Micromech. Microeng.* **2010**, *20*, 105008. [CrossRef]
40. Ahmed, D.H.; Park, H.B.; Sung, H.J. Optimum geometrical design for improved fuel utilization in membraneless micro fuel cell. *J. Power Sources* **2008**, *185*, 143–152. [CrossRef]
41. Bazylak, A.; Sinton, D.; Djilali, N. Improved fuel utilization in microfluidic fuel cells: A computational study. *J. Power Sources* **2005**, *143*, 57–66. [CrossRef]
42. Krishnamurthy, D.; Johansson, E.O.; Lee, J.W.; Kjeang, E. Computational modeling of microfluidic fuel cells with flow-through porous electrodes. *J. Power Sources* **2011**, *196*, 10019–10031. [CrossRef]
43. Wang, H.N.; Zhu, X.; Zhang, B.; Ye, D.D.; Chen, R.; Liao, Q.; Sui, P.C.; Djilali, N. Two-phase computational modelling of a membraneless microfluidic fuel cell with a flow-through porous anode. *J. Power Sources* **2019**, *420*, 88–98. [CrossRef]
44. Shyu, J.C.; Wei, C.S.; Lee, C.J.; Wang, C.C. Investigation of bubble effect in microfluidic fuel cells by a simplified microfluidic reactor. *Appl. Therm. Eng.* **2010**, *30*, 1863–1871. [CrossRef]
45. Helton, J.C.; Davis, F.J. Latin hypercube sampling and the propagation of uncertainty in analyses of complex systems. *Reliab. Eng. Syst. Saf.* **2003**, *81*, 23–69. [CrossRef]
46. MATLAB. *The Language of Technical Computing-Release 14*; Mathworks: Natick, MA, USA, 2004.
47. Xie, T.; Yu, H.; Wilamowski, B. Comparison between Traditional Neural Networks and Radial Basis Function Networks. In Proceedings of the IEEE International Symposium on Industrial Electronics, Gdansk, Poland, 27–30 June 2011; pp. 1194–1199. [CrossRef]
48. Burak, O.; Tolbert, L.M.; Chiasson, J.N. Harmonic Optimization of Multilevel Converters Using Genetic Algorithms. In Proceedings of the IEEE 35th Annual Power Electronics Specialists Conference, Aachen, Germany, 20–25 June 2004. [CrossRef]
49. Roache, P.J. Verification of Codes and Calculations. *AIAA J.* **1998**, *36*, 696–702. [CrossRef]
50. Wang, Y.; Luo, S.; Kwok, H.Y.H.; Pan, W.; Zhang, Y.; Zhao, X.; Leung, D.Y.C. Microfluidic fuel cells with different types of fuels: A prospective review. *Renew. Sustain. Energy Rev.* **2021**, *141*, 110806. [CrossRef]
51. Liu, C.; Liu, H.; Liu, L. Potassium Permanganate as an Oxidant for a Microfluidic Direct Formate Fuel Cell. *Int. J. Electrochem. Sci.* **2019**, *14*, 4557–4570. [CrossRef]